ACS Biomaterials SCIENCE & ENGINEERING
Cite This: ACS Biomater. Sci. Eng. 2019, 5, 1141−1149
Article
pubs.acs.org/journal/abseba

Resemblance in Corrosion Behavior of Selective Laser Melted and Traditional Monolithic β Ti-24Nb-4Zr-8Sn Alloy

Peng Qin,[†] Yang Chen,[‡] Yu-Jing Liu,[†] Junxi Zhang,[‡] Liang-Yu Chen,[†,§] Yuhua Li,[∥] Xuhui Zhang,[∥] Chongde Cao,[*,⊥] Hongqi Sun,[†] and Lai-Chang Zhang[*,†]

[†]School of Engineering, Edith Cowan University, 270 Joondalup Drive, Joondalup, Perth, Western Australia 6027, Australia
[‡]Shanghai Key Laboratory of Material Protection and Advanced Material in Electric Power, Shanghai University of Electric Power, Shanghai 200090, China
[§]School of Science, Jiangsu University of Science and Technology, Zhenjiang, Jiangsu 212003, China
[∥]School of Mechanical Engineering, Xi'an University of Science and Technology, Xi'an 710054, China
[⊥]Department of Applied Physics, Northwestern Polytechnical University, Xi'an 710072, China

ABSTRACT: Distinct corrosion behavior was reported in multiphased titanium alloys prepared by additive manufacturing and by traditional technologies because of different phase constituents formed during processing. An open question is therefore raised: is there always different corrosion behavior of materials prepared by different methods? This work reports resemble corrosion behavior of selective laser melted and wrought single β-phase Ti-24Nb-4Zr-8Sn (Ti2448) in both NaCl solution and Hank's solution. The electrochemical measurements showed that both samples have close calculated polarization resistance and corrosion potential in NaCl solution, i.e., 4.99 ± 0.63 MΩ cm^2 and −0.26 ± 0.01 V for the selective laser-melted Ti2448, and 4.42 ± 0.71 MΩ cm^2 and −0.25 ± 0.01 V for the wrought Ti2448, respectively. Both samples reveal the same variation in weight change after 180-day immersion test in Hank's solution. Such resemblance in corrosion behavior without pitting morphologies is attributed to the formation of monolithic β-phase during processing, which demonstrates that titanium alloys with single phase show comparable corrosion behavior regardless of the manufacturing methods adopted.

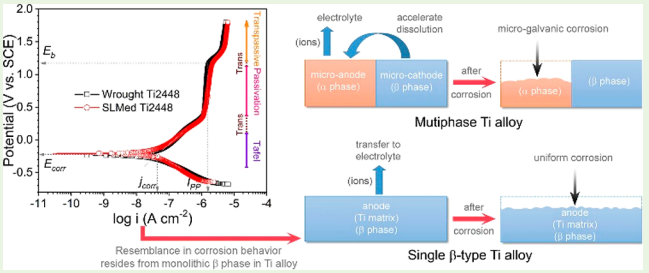

KEYWORDS: *selective laser melting, corrosion behavior, resemblance, beta phase, titanium alloy*

1. INTRODUCTION

Thanks to a considerable number of advantages in light weight, good mechanical properties, good corrosion resistance, and excellent biocompatibility, titanium (Ti) alloys have been applied as biomedical implant materials for many years.[1−7] Ti alloys are generally prepared by solidification/casting, powder metallurgy, space holder technology, and foaming.[8−11] However, biomedical implants often have complex shapes and their sizes are varied for specific patients. Therefore, the manufacturing of biomedical implants by using conventional technologies always have significant time, material, and energy costs.[12−14] Fortunately, additive manufacturing (AM), as a new type of emerging technology, has been employed to solve the traditional manufacturing problems of Ti alloys.[15−17]

Among the AM technologies, selective laser melting (SLM) and electron beam melting (EBM) are the two most frequently used AM techniques for producing metal materials; these AM techniques use a computer-controlled heat source (laser or electron beam, respectively) to manufacture Ti alloy parts with complex shapes.[16,18] The resultant SLM-produced (SLMed) or EBM-produced (EBMed) Ti alloy parts have been reported to exhibit comparable or even better mechanical properties compared with their counterparts produced by traditional processing methods.[19−21] For example, Zhang et al.[22] compared the mechanical properties of commonly used Ti-6Al-4V (in wt %, the same hereafter unless otherwise indicated) produced by SLM and casting methods. The results demonstrate the enhanced mechanical properties of SLMed Ti-6Al-4V in terms of Vickers hardness (409 HV), yield strength (1110 MPa) and ultimate tensile strength (1267 MPa) compared with the corresponding ones for the cast counterparts (i.e., Vickers hardness of 346 HV, yield strength of 847 MPa and ultimate tensile strength of 976 MPa). Additionally, SLMed Ti-24Nb-4Zr-8Sn (indicated as Ti2448 hereafter) also exhibits desirable Young's modulus of 53 GPa, yield strength of 563 GPa, and ultimate tensile strength of 665 GPa.[17,23] The Young's moduli for the EBM-produced porous Ti2448 with different porosities have been decreased to 1 GPa (at porosity of 79.5%) and 1.34 GPa (at porosity of 75%).[19,24] In such a case, the EBMed porous Ti2448 with low Young's modulus could effectively reduce the stress shielding effect in the human body when an implant made of Ti2448 alloy is

Received: October 29, 2018
Accepted: December 19, 2018
Published: December 19, 2018

DOI: 10.1021/acsbiomaterials.8b01341
ACS Biomater. Sci. Eng. 2019, 5, 1141−1149

used. Such results show that the Ti alloys produced by AM techniques can meet the demand for industrial and biomedical purposes in terms of their mechanical properties.

However, considering the environments in which AM-produced Ti alloys are employed, the corrosion behavior of AM-produced Ti alloys in corrosive media is another significant criterion for biomedical applications. In general, corrosion of biomedical implants takes place due to galvanic corrosion on the contact surfaces of different metals or metal/tissue interfaces, which may cause inflammation and even lesions within the human body.[25−27] Very recently, several reports have addressed the corrosion behavior of AM-produced Ti alloys. For example, Dai et al.[28] and Wu et al.[8] found that the formation of acicular α' phase degrades the corrosion resistance of the SLMed Ti-6Al-4V and wire arc additive manufactured Ti-6Al-4V in NaCl solution compared with the commercial Ti-6Al-4V alloy, respectively. Dai et al.[29] further showed that a larger percentage of acicular α' phase would degrade the corrosion resistance of SLMed Ti-6Al-4V. By contrast, Bai et al.[30] indicated that the EBMed Ti-6Al-4V composed of refined α and β phase has slightly better corrosion resistance than the wrought counterpart, which is attributed to a higher volume fraction of β phase formed in the EBMed Ti-6Al-4V and/or the formation of α phase in EBMed Ti-6Al-4V alloy instead of α' phase in the microstructure of SLMed counterpart. In the meantime, Gong et al.,[31] Li et al.[10,32] and Chiu et al.[33] respectively investigated the effect of different phase fraction on the corrosion resistance of EBMed, laser solid formed (another AM technique) and direct metal printed (another AM technique) Ti-6Al-4V, and found the samples with a lower fraction of α phase or a higher fraction of β phase have better corrosion resistance. However, Dai et al.[34] elucidated that the corrosion resistance of the SLMed Ti-6Al-4V is still unfavorable even through the transformation of α' phase to α phase and/or the augment of β phase by heat treatment. From the above studies, it seems that there is little consensus of critical significance on the corrosion performance of the AM-produced Ti-6Al-4V. One can note that the Ti-6Al-4V studied in the previous work are always composed of various phases (such as α, α' and β phases). The distinct preparation methods can result in different phase constituents in Ti-6Al-4V alloy. The other AM-produced alloys, such as Al−Si alloys, also present different phase constituents compared with the ones in the counterparts prepared by the traditional methods. For example, more refined Si particles in the SLMed Al−Si alloys could prominently enhance the corrosion resistance.[35,36] Hence, it is still unclear whether the AM-produced alloys have better or worse corrosion resistance compared with their traditional counterparts. Therefore, an open question arises: how is the corrosion resistance of a Ti alloy (and other alloys as well) with the same phase constituents (such as single phase) prepared by AM technique compared with the traditional counterpart? Unfortunately, there is still a lack of existing investigation to answer this open question. A better understanding of the corrosion resistance of single-phase alloys prepared by AM technique and traditional methods is urgently needed.

In our previous studies, the SLM-produced Ti-6Al-4 V has been extensively studied.[28−30,34] We confirmed that pitting corrosion is prone to take place in such a biphasic Ti alloy both prepared by SLM and traditional methods, degrading the corrosion resistance of the Ti alloys. These results motivate us to investigate the corrosion behavior of singe-phase Ti alloys. Among Ti alloys, Ti2448 alloy, as one of the potential β-type biomedical materials, has been successfully produced by SLM[12,16] and by EBM.[18,19,24] Therefore, a SLMed Ti2448 alloy was selected as the experimental alloy, and a wrought Ti2448 alloy was used as a reference in this work. Considering the biomedical applications of Ti2448, electrochemical measurements, immersion tests, and microstructural characterizations were conducted to investigate the corrosion behavior of the experimental alloys. The results elucidate that without the microgalvanic effect triggered by heterogeneous phases, the corrosion behavior of the SLMed Ti2448 would be comparable to that of the wrought counterpart.

2. EXPERIMENTAL SECTION

2.1. Materials Preparation. Two types of Ti2448 cubes (10 mm × 10 mm × 10 mm) from different manufacturing methods were used in this work: Ti2448 produced by SLM technique (indicated as SLMed Ti2448) and wrought Ti2448 (indicated as wrought Ti2448). The powder used for SLMed Ti2448 was prepared by a gas atomized from a remolten Ti2448 ingot in a vacuum arc furnace. The produced powder particles had a spherical shape with the diameter ranging from 45 to 100 μm. The SLMed Ti2448 cubes were produced using a ReaLizer SLM 100 machine equipped with a 200 W Yb: YAG fiber laser. The main SLM manufacturing parameters of Ti2448 were listed in Table 1. The scanning strategy of SLM of Ti2448 was zigzag pattern, the scanning direction was rotated 90° between each consecutive layer. The relative density, measured using the Archimedes method, of the produced Ti2448 was 99.3%. The wrought Ti2448 sample was directly cut from a wrought ingot. The prepared samples were then welded with copper wires and sealed in epoxy resin. Subsequently, the sample surface was mechanically ground up to 2000 grits using SiC paper and polished with a colloidal silica suspension to a 0.04 μm with a mirror finish. The polished samples were ultrasonically cleaned with ethanol for 3 min and then air-dried.

Table 1. Main SLM Manufacturing Parameters Used in This Work

parameter	value
laser power (W)	200
laser scan speed (mm s^{-1})	750
laser spot size (μm)	40
layer thickness (μm)	50
hatch space (μm)	100
energy density (J mm^{-3})	80

2.2. Phase Identification and Microstructure Characterizations. X-ray diffraction (XRD, PANalytical Empyrean diffractometer) was used to study the phase constituents of the samples using Co−K_α radiation at room temperature. The XRD was performed with a scan rate of 0.03° s^{-1} from 30° to 110°. The experimental data were analyzed by the Software of X'pert Highscore Plus with PAN-ICSD database. The surface morphologies of SLMed Ti2448 and wrought Ti2448 before and after corrosion tests were measured by a Zeiss optical microscope and a field emission scanning electron microscope (FE-SEM, JSM-7800F, JEOL). A Kroll's solution, composed of 2 vol % HF (concentration 48−51%, CAS Number 7664-39-3, Sigma-Aldrich), 6 vol % HNO_3 (concentration 70%, CAS Number 7697-37-2, Sigma-Aldrich), and 92 vol % H_2O, was used to etch the alloy samples for microstructural characterization purpose.

2.3. Electrochemical Measurements. The electrochemical tests in this work were carried out in a 3.5 wt.% NaCl (purity ≥99.5%, CAS Number 7647-14-5, Sigma-Aldrich) solution at room temperature (about 24 °C) with a Gamry 6000 electrochemical workstation, coupled with a conventional three-electrode system (ASTM G3-89).

DOI: 10.1021/acsbiomaterials.8b01341
ACS Biomater. Sci. Eng. 2019, 5, 1141−1149

The working electrode of this system was the experimental alloy, a platinum net was used as the counter electrode, and a saturated calomel electrode (SCE) was used as the reference electrode. Accordingly, the electrochemical potentials reported in this work were referred to SCE. Prior to the electrochemical impedance spectrum (EIS) test, an open circuit potential (OCP) measurement for 70h was conducted to obtain a relatively stable state for each tested sample. The frequency range of the EIS test was between 1×10^4 Hz and 1×10^{-2} Hz with a low amplitude alternating current amplitude of 5 mV. Finally, the potentiodynamic polarization was tested based on the relatively stable state after the EIS test. The potential scanning range was from −0.25 V versus the OCP to +1.80 V at a sweep rate of 0.1667 mV s^{-1}. The experiments were repeated at least three times to ensure data reproducibility.

2.4. Immersion Tests. Three pieces of sample sheets for each type of Ti2448 were prepared for immersion test in simulated body fluid (Hank's balanced salts: MDL number MFCD00217418, Sigma-Aldrich) at 37 °C. The simulated body fluid (Hank's solution) in the immersion test was adjusted by adding 0.35 g L^{-1} $NaHCO_3$ (purity ≥99.5%, CAS Number 144-55-8, Sigma-Aldrich), and the other main compositions of Hank's solution were 0.140 g L^{-1} $CaCl_2$, 0.098 g L^{-1} $MgSO_4$, 0.4 g L^{-1} KCl, 0.06 g L^{-1} KH_2PO_4, 8 g L^{-1} NaCl, 0.048 g L^{-1} Na_2HPO_4, 1 g L^{-1} $C_6H_{12}O_6$, and 0.011 g L^{-1} $C_{19}H_{14}O_5SNa$. The final pH value of Hank's solution was modified by adding the diluted HCl solution (concentration 36.5−38.0%, CAS Number 7647-01-0, Sigma-Aldrich) and diluted NaOH (purity ≥98%, CAS Number 1310−73−2, Sigma-Aldrich) solution to reach 7.4. The size of each sample for immersion test was 10 mm × 10 mm × 1 mm with a total immersion period of 6 months. Surface morphologies of the immersed samples were then studied using optical microscopy, and the weight analysis of these samples was carried out after removing the corrosion product using the wash solution consisted of 70 mL of HNO_3 (concentration 70%, CAS Number 7697-37-2, Sigma-Aldrich) and 30 mL of H_2O.

3. RESULTS

3.1. Phase Constituent and Microstructural Feature. Figure 1a shows the XRD patterns for the SLMed Ti2448 and wrought Ti2448. The result shows a board range of peaks at 44.9°, 65.4°, 82.9°, and 99.6° for both samples, corresponding to (011), (002), (112), and (022) planes of β phase in Ti (ICSD 44391), respectively. The above result indicates that both experimental alloys have a single body-centered cubic (BCC) structure. The crystallographic data extracted from the software of Jade 6.5 are 0.33037 and 0.33095 nm for SLMed Ti2448 and wrought Ti2448, respectively, which are significantly close to the crystallographic data of pure BCC Ti (0.33065 nm). The optical microstructures of the etched SLMed Ti2448 and wrought Ti2448 are revealed in Figures 1b, c. The SLMed Ti2448 shows a lot of SLM scan tracks associated with small grains. The wrought Ti2448 presents several processing flows accompanied with fragmentary grains, indicating an incomplete recrystallized state. Furthermore, the grain size in SLMed Ti2448 is significantly smaller than that in wrought Ti2448. Some studies indicated that the refined microstructure would improve the corrosion resistance of an alloy.[30,35−37] For example, the refined α grain of Ti-6Al-4 V produced by EBM enhances the corrosion resistance compared with the wrought counterpart; the refined Si particles of Al-12Si produced by SLM significantly minimize the micro-galvanic effect of the coarse Si particles in the cast counterpart, thereby improving the corrosion resistance.

3.2. Electrochemical Measurements. The OCP results for 70 h immersion in 3.5 wt.% NaCl solution are shown in Figure 2. The OCP curves show distinct fluctuations at the initial stage of the tests. Such a phenomenon results from the

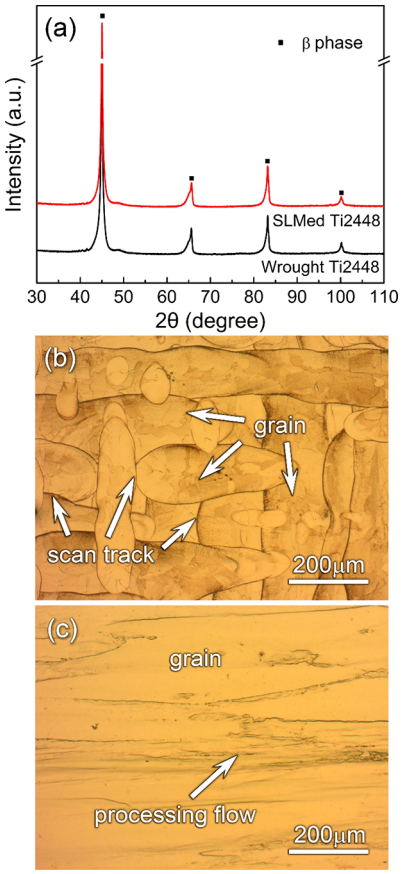

Figure 1. (a) XRD patterns for the selective laser melted Ti2448 and wrought Ti2448; and optical microstructures of: (b) selective laser melted Ti2448 and (c) wrought Ti2448. Ti2448 indicates Ti-24Nb-4Zr-8Sn.

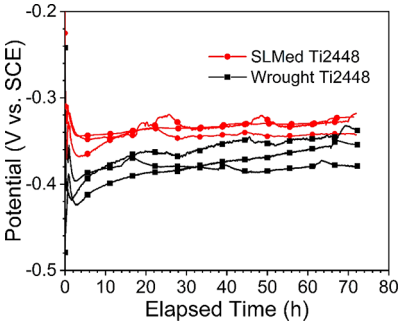

Figure 2. OCP vs time for the selective laser melted Ti2448 and wrought Ti2448 immersed in 3.5 wt.% NaCl solution at room temperature. The final relatively stable OCPs for both samples are between −0.3 and −0.4 V, indicating no significant difference in OCP between these two samples. Ti2448 indicates Ti-24Nb-4Zr-8Sn.

transfer of electrons between the metal surface and the solution at the beginning of the immersion of the working electrode in the corrosive environment until an equilibrium of electrochemical potential is reached for both sides.[37] Dai et al.[28,29] also mentioned that the formation of the passive film on the surface of the electrode would result in a suppressed anodic process and a positive shifted potential. Therefore, two distinct stages can be found in Figure 2 for both SLMed Ti2448 and wrought Ti2448. The first stage is the quick dissolution in the first 2 h, which is indicated by the large drops of the OCP curves. The second stage is the formation of the passive film on

DOI: 10.1021/acsbiomaterials.8b01341
ACS Biomater. Sci. Eng. 2019, 5, 1141−1149

the surface of the electrode. In the second stage, a relative stabilized positive shift is observed on the OCP curve until the 70th hour. The final relatively stable OCPs for SLMed Ti2448 and wrought Ti2448 are between −0.3 V and −0.4 V, which indicates that there is no prominent OCP difference between the SLMed Ti2448 and wrought Ti2448 samples.

Figure 3 reveals the EIS results of SLMed Ti2448 and wrought Ti2448. The Nyquist plots in Figure 3a show that

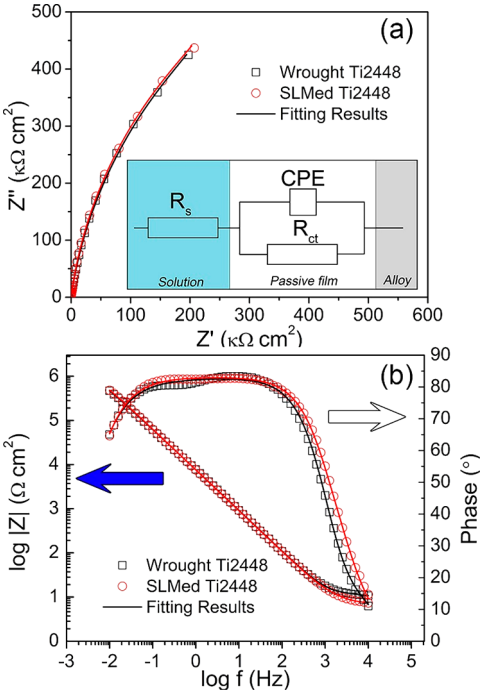

Figure 3. EIS results of selective laser melted Ti2448 and wrought Ti2448 immersed in 3.5 wt.% NaCl solution at room temperature: (a) Nyquist plots (the inset is the equivalent circuit diagram) and (b) Bode plots (the solid blue arrow indicates the Bode impedance plot and the hollow arrow illustrates the Bode phase angle plot). Ti2448 indicates Ti-24Nb-4Zr-8Sn.

both SLMed Ti2448 and wrought Ti2448 only consist of a considerable large semicircle, and the semicircles have a nearly identical radius, which is consistent with the similar charge transfer resistance (R_{ct}) from the EIS fitting results in Table 2. The radius of semicircle presented in the Nyquist plot usually indicates the impedance of the formed oxide film on the sample surface.[28−30,34,38] Generally, a larger radius of the semicircle means a denser oxide formed on samples surface with higher impedance, which results in better corrosion resistance of the sample.[39−42] The similar semicircle radii of the tested samples in this work illustrate the approximated impedances of the formed oxide films on both SLMed Ti2448 and wrought Ti2448. The Bode impedance plots in Figure 3b (as indicated by solid blue arrow) reveals two distinct regions for both SLMed Ti2448 and wrought Ti2448. The nearly flat part in the high-frequency range corresponds to the solution resistance. Then the impedance increases up to 1×10^6 Ω cm^2 in the following frequency range between 1×10^3 Hz and 1×10^{-2} Hz. Meanwhile, in the bode phase angle plot (as indicated by hollow arrow), a wide plateau of phase angle above 70° is represented between the frequency range of 1×10^2 Hz and 1×10^{-1} Hz in Figure 3b, explaining a dense passive film formed

Table 2. Fitting Results of EIS for the SLMed Ti2448 and Wrought Ti2448 Immersed in 3.5 wt % NaCl Solution

	R_s (Ω cm^2)	CPE ($\times 10^{-4}$ Ω^{-1} cm^{-2} S^{-n})	n	R_{ct} (MΩ cm^2)	χ^2
SLMed Ti2448	5.77	2.95	0.94	3.83	0.0006
	7.25	4.12	0.92	1.60	0.0004
	5.82	4.53	0.93	1.03	0.0007
average	6.28	3.87	0.93	2.15	0.0006
standard deviation	0.84	0.82	0.01	1.48	0.0001
wrought Ti2448	6.43	2.73	0.94	1.74	0.0007
	10.67	4.08	0.92	1.50	0.0007
	6.34	3.97	0.91	3.34	0.0015
average	7.81	3.59	0.93	2.19	0.0010
standard deviation	2.47	0.75	0.02	1.00	0.0004

[a] R_s and R_{ct} are the fitted solution resistance and charge transfer resistance, respectively; CPE is the constant phase element; n corresponds to the deviation from capacitor; χ^2 indicates the fitting quality between the experiment data and the fitting data.

on the sample surface for both SLMed Ti2448 and wrought Ti2448.[43−45]

It was indicated that the oxide film formed on the surface of the experimental alloys could be composed of a dense inner layer and a porous outer layer.[43] Therefore, after considering with the EIS results in this work and the reported results from the literature,[28,38,46] an electrical equivalent circuit diagram (model of $R(QR)$) was chosen to fit the EIS results. The schematic drawing of the layer and the equivalent circuit diagram is shown in Figure 3a inset. The components of the equivalent circuit diagram include a solution resistance (R_s), a constant phase element (CPE), and a charge transfer resistance (R_{ct}). The CPE is used instead of capacitance because the distribution of the electric is nonuniform and the outer layer of passive film formed on the sample surface could increase the surface roughness.[47,48] Accordingly, the fitting results of n in Table 2 represent the deviation from ideal capacitor,[43] which indicates an ideal capacitor response in the system if the fitted value n is close to 1. The other fitting results, such as R_s, are much smaller than R_{ct}, in which the effect of the solution resistance is significantly small or the corrosion resistance of the samples in this system is mainly affected by the density of the oxide film formed on the sample surface. Furthermore, the R_{ct} means the transferability of the ions between the electrode surface and the electrolyte; the higher value of the R_{ct} illustrates less charge transfer between the electrode surface and the electrolyte and lower corrosion rate of the sample.[28,29,38] The value of R_{ct} for the wrought Ti2448 is only 2.19 ± 1.00 MΩ cm^2, which is slightly higher than that for the SLMed Ti2448 (2.15 ± 1.48 MΩ cm^2) and is within the standard deviation.

The potentiodynamic polarization curves for the SLMed Ti2448 and wrought Ti2448 are shown in Figure 4. An evident passivation region is observed in this figure for both samples and divides the whole potentiodynamic curve into three typical regions: a Tafel region, a passivation region, and a transpassive region. The corrosion current density (j_{corr}) and corrosion potential (E_{corr}) could be calculated by fitting the Tafel region.[29,38] For example, the j_{corr} and E_{corr} could be obtained by fitting two tangent lines in Tafel region (as shown in Figure 4). The intersections in x-axis and y-axis corresponds to j_{corr} and E_{corr}, and the slopes of these two tangent lines are the β_a and

DOI: 10.1021/acsbiomaterials.8b01341
ACS Biomater. Sci. Eng. 2019, 5, 1141−1149

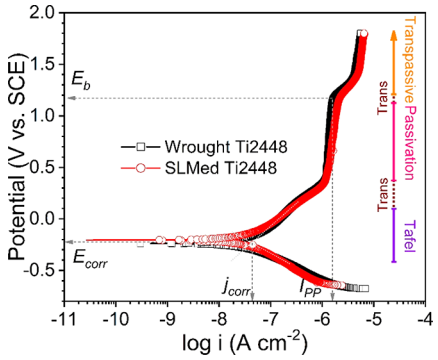

Figure 4. Potentiodynamic polarization curves for the selective laser melted Ti2448 and wrought Ti2448 immersed in 3.5 wt % NaCl solution. Ti2448 indicates Ti-24Nb-4Zr-8Sn.

β_c. The polarization resistance (R_p) could be calculated by using the following equation:[49,50]

$$R_p = \frac{\beta_a|\beta_c|}{2.303(\beta_a + |\beta_c|)}\frac{1}{j_{corr}} \quad (1)$$

The corresponding results are listed in Table 3. It is clear that the average values of the corrosion current densities for the

Table 3. Fitting Results of Potentiodynamic Polarization Curves for the SLMed Ti2448 and Wrought Ti2448 Immersed in 3.5 wt % NaCl Solution

	β_a (mV)	β_c (mV)	j_{corr} (μA cm^{-2})	E_{corr} (V)	R_p (MΩ cm^2)
SLMed Ti2448	334	72	0.0055	−0.26	4.74
	278	113	0.0077	−0.25	4.52
	278	74	0.0045	−0.26	5.71
average	297	86	0.0059	−0.26	4.99
standard deviation	32	22	0.0017	0.01	0.63
wrought Ti2448	214	130	0.0078	−0.24	4.51
	117	123	0.0071	−0.26	3.67
	294	110	0.0069	−0.25	5.08
average	209	121	0.0073	−0.25	4.42
standard deviation	88	10	0.0005	0.01	0.71

[a] β_a and β_c are the fitting anode and cathode slope of Tafel region, respectively; j_{corr} is the fitted corrosion current density; E_{corr} is the corrosion potential, and R_p is the calculated polarization resistance.

SLMed Ti2448 and wrought Ti2448 are 0.0059 ± 0.0017 μA cm^{-2} and 0.0073 ± 0.0005 μA cm^{-2}, respectively. In addition, the polarization resistance of each sample in the potentiodynamic polarization test can also be calculated.[46] The calculated polarization resistance indicates that both materials have an approximated polarization resistance, i.e., 4.99 ± 0.63 MΩ cm^2 for the SLMed Ti2448 and 4.42 ± 0.71 MΩ cm^2 for the wrought Ti2448. In the meantime, the same corrosion potential (E_{corr}) of −0.25 V is found for the SLMed Ti2448 and wrought Ti2448. In the passivation region, the passivation potential ranges from 0.35 to 1.2 V for both samples. There is no pitting phenomenon observed within the passivation region, this is confirmed by no sudden increase in corrosion current density without any potential changes in the passivation region. Furthermore, the passivation current density (I_{PP}) of the SLMed Ti2448 is almost the same as that of the wrought Ti2448, where the values are around 1.41 μA cm^{-2} for both samples. Above the passivation region, the current density begins to increase as the potential passes over 1.2 V (E_b, breakdown potential). The passivation at this stage is considered as a temporary finish, and the Cl^- reaches the metal surface.[34,38] Afterward, quick secondary passivation is observed above the breakdown potential, which illustrates both materials have a robust repassivation ability of oxide film.

Figure 5 shows the SEM morphologies of SLMed Ti2448 and wrought Ti2448 before and after electrochemical tests. It is distinct that the surface morphologies of both samples are similar. No significant corrosion trace and pitting could be found on both sample surface except for the intrinsic defects in the SLMed Ti2448. This phenomenon indicates that both SLMed Ti2448 and wrought Ti2448 are corrosion-resistant to NaCl solution. Such similar surface morphologies of both samples also demonstrate their similar electrochemical behavior in this work.

3.3. Immersion Tests. After 180-days of immersion in Hank's solution, the morphology of mixed oxide film and corrosion products were obtained for all immersed samples. The optical microscopy observations (Figure 6) indicate that large quantities of pellet-like corrosion products are observed for both SLMed Ti2448 and wrought Ti2448 samples. Such a result illustrates that it is difficult to find any difference in the morphologies of both immersed samples. After removing the oxide film and corrosion product, the immersed SLMed Ti2448 and wrought Ti2448 samples also have the almost same weight (1.432 ± 0.005 g for the SLMed Ti2448 and 1.570 ± 0.005 g for the wrought Ti2448, respectively) compared with the sample weight before the immersion test (the original sample weight is 1.432 ± 0.005 g for the SLMed Ti2448 and 1.570 ± 0.005 g for the wrought Ti2448, respectively). This elucidates that the spontaneous passivation film (such as the TiO_2 and Nb_2O_5[38,47]) formed on Ti2448 is stable and resistant to corrosion in Hank's solution. Therefore, the immersion test results are in line with the electrochemical results, where the SLMed Ti2448 and wrought Ti2448 with single β-phase have a similar and strong resistance to corrosion in 3.5 wt % NaCl solution.

Figure 7 shows the SEM image of the cross-section of the corroded samples after 180-day immersion in Hank's solution at 37 °C. The figure shows three distinct regions for all tested samples, including resin on top, corrosion products mixed with an oxide film in the middle, and the substrate on the bottom. It is significant that the corrosion products formed on the SLMed and wrought Ti2448 have the similar thicknesses of around 3 μm. Such a result elucidates the resemble corrosion behavior of the SLMed and wrought Ti2448. If both samples have a distinctive corrosion mechanism, they would possess rather different corrosion products in morphology. Therefore, the outcomes of the immersion test are consistent with the results of the electrochemical measurements.

4. DISCUSSION

Galvanic corrosion is one of the most common corrosion types for alloys in electrolyte solutions, which always results from the formation of (micro-)galvanic couple due to the potential difference between the anode phase and cathode phase.[51] In general, the microgalvanic couple in multiphase Ti alloys could cause severe corrosion in the anode phase. Taking examples from the literature,[30,34,38,46,52] the corrosion mechanism of multiphase or single-phase Ti alloys prepared by SLM can be understood further. Ti-6Al-4V alloy is a typical dual-phase Ti

DOI: 10.1021/acsbiomaterials.8b01341
ACS Biomater. Sci. Eng. 2019, 5, 1141−1149

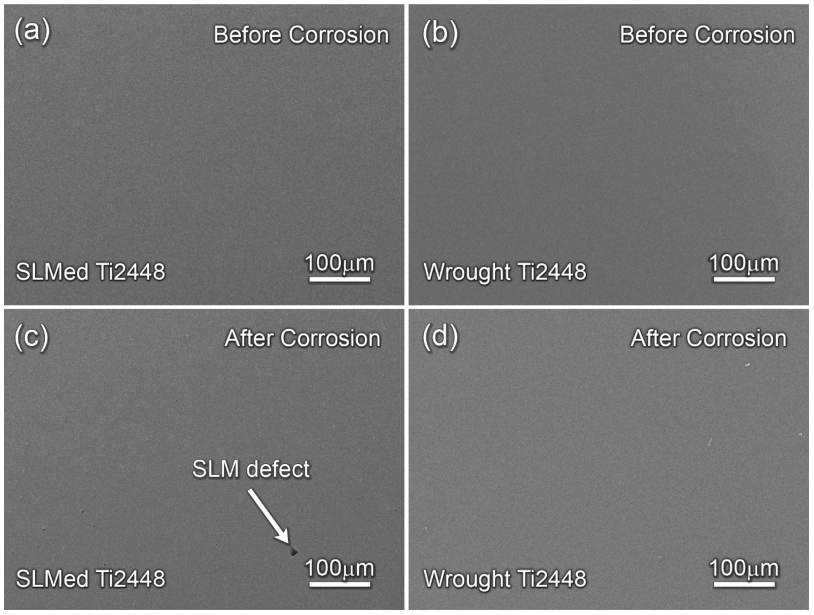

Figure 5. Secondary electron SEM images of (a) selective laser melted Ti2448 and (b) wrought Ti2448 before electrochemical corrosion test in NaCl solution, and (c) selective laser melted Ti2448 and (d) wrought Ti2448 after electrochemical corrosion test in NaCl solution. No distinctive corrosion is found for both alloys. Ti2448 indicates Ti-24Nb-4Zr-8Sn.

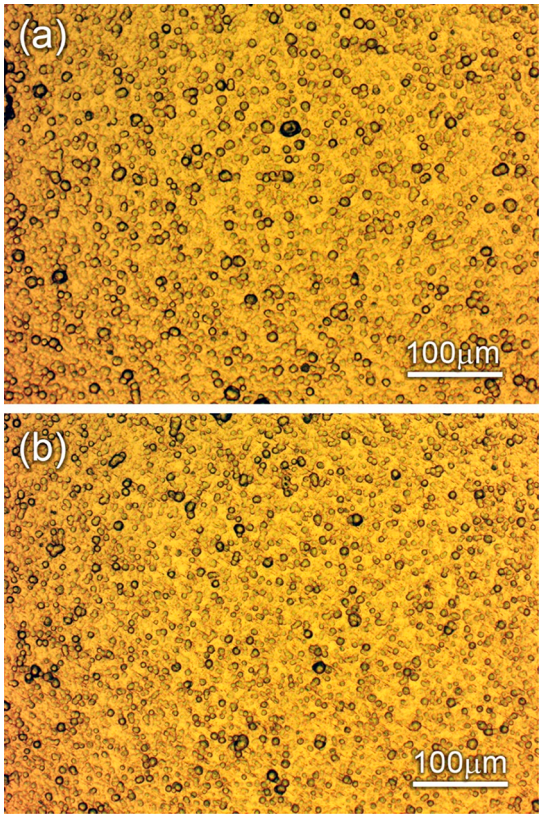

Figure 6. Surface morphologies of (a) selective laser melted Ti2448 and (b) wrought Ti2448 after 180-day immersion in Hank's solution. No distinctive corrosion morphologies are found for both alloys. Ti2448 indicates Ti-24Nb-4Zr-8Sn.

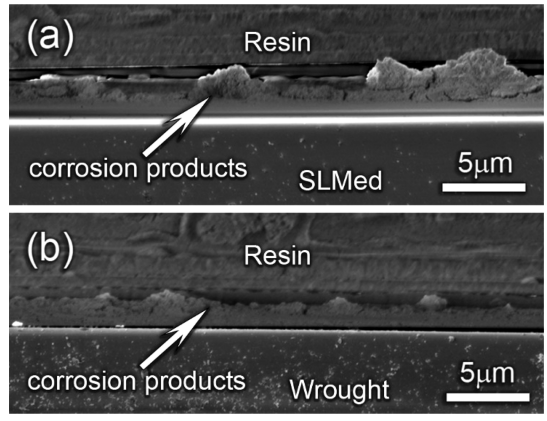

Figure 7. SEM image of the cross-section of the corroded samples: (a) selective laser melted Ti2448 and (b) wrought Ti2448 after 180-days immersion in Hank's solution at 37 °C.

alloy which consists of the α (or α') phase and β phase.[28,30,34] Figure 8a gives the schematic illustration of the corrosion mechanism by using the model of a galvanic microcell for Ti-6Al-4V alloy. The microgalvanic corrosion process takes place between the α phase and β phase. During the corrosion, the α phase containing the α-stabilizer (e.g., Al) would act as the microanode, and the β phase containing the β-stabilizer (e.g., V) would act as the microcathode. Due to the electrochemical reaction, the microcathode accelerates the dissolution of the microanode where especially dissolves the spontaneous oxide film formed on the sample surface.[53] In this case, as revealed in Figure 8a, severe pitting corrosion takes place in the microanode. Therefore, galvanic corrosion is commonly found in the SLMed Ti-6Al-4V. This is especially significant because of the fast cooling rate; the large generated amount of acicular α' phase with high energy state, which acted as the microanode, is more prone to be corroded in the SLMed Ti-6Al-4V.[29] A similar scenario is elucidated in the SLMed Ti-5Cu alloy in our previous study; The microcathode of Ti matrix would tremendously accelerate the dissolution of the small amount of microanode α' phase presented in the boundaries of melting pools.[46]

DOI: 10.1021/acsbiomaterials.8b01341
ACS Biomater. Sci. Eng. 2019, 5, 1141−1149

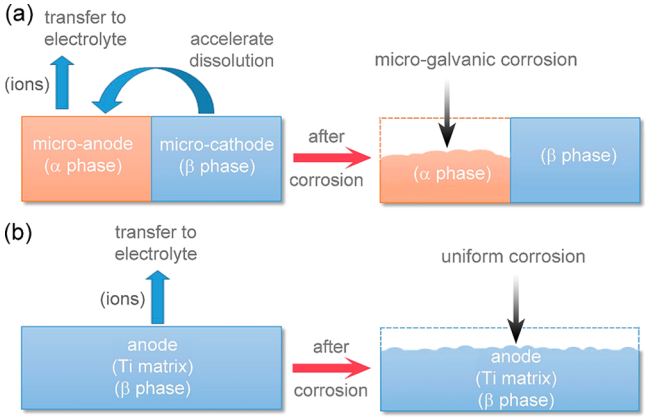

Figure 8. Corrosion mechanism of: (a) dual phase Ti alloy, and (b) single β-phase Ti alloy. Because of the existence of a heterogeneous phase, the microgalvanic effect is prone to form and accelerates the dissolution of microanode in dual-phased Ti alloy. Therefore, severe pitting corrosion is always found in dual-phase Ti alloy. By contrast, microgalvanic effect between different phases is absent in single β-phase Ti alloy. Hence, only uniform corrosion is observed.

However, the β-type Ti2448 alloy only consists of the single β-phase that eliminates the effect of the microgalvanic couple between the different phases during corrosion. As shown in Figure 8b, the Ti2448 alloys (both for SLMed Ti2448 and wrought Ti2448) would be corroded simultaneously without prior microgalvanic corrosion between the different phases. Hence, the corrosion of the β-type Ti2448 alloy potentially occurs at the grain boundaries where the lattice mismatch is presented and in the high-energy state.[51] However, the passivation abilities of Ti and Nb elements in Ti2448 alloy are extremely strong that could generate a spontaneous passivation film (such as Nb_2O_5 and TiO_2) and greatly prevent the corrosion at the grain boundaries.[38,47,51] Therefore, no evident pitting corrosion could be found in the morphology of the corroded SLMed Ti2448 and wrought Ti2448 after immersion tests. Similar to the study of Navarro Laboulais et al.,[54] the corrosion resistance of the β-type Ti35Nb10Ta-xFe alloys produced by powder metallurgy method does not change significantly with increasing the Fe concentration in 1 M H_2SO_4 solution, and there is no film breakdown phenomenon up to 2 V for all tested samples during the potentiodynamic polarization. Bai et al.[55] studied the corrosion behavior of hot-rolled β-type Ti45Nb alloy under different solutions. The result demonstrates that the Ti45Nb has an excellent corrosion resistance in simulated body fluid and Fusayama−Meyer artificial saliva solution but not in fluoridated acidified artificial saliva solution. There is also no film breakdown up to 3 V for all tested samples during the potentiodynamic polarization, suggesting the occurrence of uniform corrosion and the formation of a spontaneous oxide film (such as TiO_2, Nb_2O_5). However, not all β-type Ti alloys have the same phenomenon. The corrosion behavior during the electrochemical test always depends on the sample surface condition, temperature, electrolyte, etc. For example, Li[52] has studied the corrosion properties of nanostructured Ti2448 alloy under different fluoride concentration. The result indicates that as the fluoride concentration increases, the corrosion resistance of the tested samples is reduced and the pitting phenomenon takes place at the fluoride concentration above 0.1%. This work confirms that the SLMed single β-phase Ti2448 alloy has comparable corrosion behavior with the counterpart manufactured by a conventional method (Figures 2−6). Thus, this work advances a new understanding for the corrosion behavior for Ti alloys prepared by SLM.

5. CONCLUSIONS

In this work, a Ti-24Nb-4Zr-8Sn (Ti2448) alloy with single β-phase was produced by selective laser melting (SLM). The corrosion behavior of the selective laser melted Ti2448 alloy was investigated by electrochemical measurements and immersion tests together with some microstructural characterizations. A wrought Ti2448 alloy was used as a reference for comparison. The main conclusions can be drawn as follows:

(1) The results from microstructural characterizations and X-ray diffraction reveal that both the selective laser melted Ti2448 and wrought Ti2448 consist of only single β-phase but different grain size. The crystallographic data extracted from the software of Jade 6.5 are 0.33037 and 0.33095 nm for SLMed Ti2448 and wrought Ti2448, respectively, which are significantly close to the crystallographic data of pure BCC Ti (0.33065 nm).

(2) The electrochemical impedance spectrum (EIS) testing result shows that the calculated polarization resistance is 2.15 ± 1.48 MΩ cm^2 for the selective laser melted Ti2448 and 2.19 ± 1.00 MΩ cm^2 for the wrought Ti2448. Meanwhile, the fitting results of potentiodynamic polarization curves indicate that the corrosion current densities for the selective laser melted Ti2448 and wrought Ti2448 are 0.0059 ± 0.0017 μA cm^{-2} and 0.0073 ± 0.0005 μA cm^{-2} and the corrosion potentials for the selective laser melted Ti2448 and wrought Ti2448 are −0.26 ± 0.02 and −0.25 ± 0.01 V, respectively. These results demonstrate that the corrosion behavior is significantly similar for the Ti2448 alloys prepared by selective laser melting and by traditional processing method.

(3) The comparable corrosion behavior of the selective laser melted Ti2448 and wrought Ti2448 is attributed to the existence of single β-phase in both alloys. Therefore, uniform corrosion is observed instead of pitting corrosion for both alloys. This work confirms that the distinction in the corrosion behavior of Ti alloys is not triggered by the manufacturing methods but by the formation of various phase constituents in the microstructure, which advances a new understanding of the corrosion behavior of Ti alloys prepared by selective laser melting.

AUTHOR INFORMATION

Corresponding Authors

*E-mail: lczhangimr@gmail.com or l.zhang@ecu.edu.au.
*E-mail: caocd@nwpu.edu.cn.

ORCID

Junxi Zhang: 0000-0001-7055-8892
Hongqi Sun: 0000-0003-0907-5626
Lai-Chang Zhang: 0000-0003-0661-2051

Notes

The authors declare no competing financial interest.

DOI: 10.1021/acsbiomaterials.8b01341
ACS Biomater. Sci. Eng. 2019, 5, 1141−1149

■ ACKNOWLEDGMENTS

The authors are grateful for the financial support from the National Key Research and Development Program (Grant 2016YFB1100101) and Australian Research Council Discovery Project (DP110101653).

■ REFERENCES

(1) Simon-Walker, R.; Romero, R.; Staver, J. M.; Zang, Y.; Reynolds, M. M.; Popat, K. C.; Kipper, M. J. Glycocalyx-inspired nitric oxide-releasing surfaces reduce platelet adhesion and activation on titanium. *ACS Biomater. Sci. Eng.* **2017**, *3*, 68−77.

(2) Mazigi, O.; Kannan, M. B.; Xu, J.; Choe, H. C.; Ye, Q. Biocompatibility and degradation of a low elastic modulus Ti-35Nb-3Zr alloy: Nanosurface engineering for enhanced degradation resistance. *ACS Biomater. Sci. Eng.* **2017**, *3*, 509−517.

(3) Agarwal, S.; Duffy, B.; Curtin, J.; Jaiswal, S. Effect of high- and low-molecular-weight hyaluronic-acid-functionalized-AZ31 Mg and Ti alloys on proliferation and differentiation of osteoblast cells. *ACS Biomater. Sci. Eng.* **2018**, *4*, 3874.

(4) Rabadia, C. D.; Liu, Y. J.; Cao, G. H.; Li, Y. H.; Zhang, C. W.; Sercombe, T. B.; Sun, H.; Zhang, L. C. High-strength β stabilized Ti-Nb-Fe-Cr alloys with large plasticity. *Mater. Sci. Eng., A* **2018**, *732*, 368−377.

(5) Rabadia, C. D.; Liu, Y. J.; Wang, L.; Sun, H.; Zhang, L. C. Laves phase precipitation in Ti-Zr-Fe-Cr alloys with high strength and large plasticity. *Mater. Des.* **2018**, *154*, 228−238.

(6) Wang, L. Q.; Xie, L. C.; Lv, Y. T.; Zhang, L. C.; Chen, L. Y.; Meng, Q.; Qu, J.; Zhang, D.; Lu, W. J. Microstructure evolution and superelastic behavior in Ti-35Nb-2Ta-3Zr alloy processed by friction stir processing. *Acta Mater.* **2017**, *131*, 499−510.

(7) Calin, M.; Zhang, L. C.; Eckert, J. Tailoring of microstructure and mechanical properties of a Ti-based bulk metallic glass-forming alloy. *Scr. Mater.* **2007**, *57*, 1101−1104.

(8) Wu, B.; Pan, Z.; Li, S.; Cuiuri, D.; Ding, D.; Li, H. The anisotropic corrosion behaviour of wire arc additive manufactured Ti-6Al-4V alloy in 3.5% NaCl solution. *Corros. Sci.* **2018**, *137*, 176−183.

(9) Ureña, J.; Tsipas, S.; Pinto, A. M.; Toptan, F.; Gordo, E.; Jiménez-Morales, A. Corrosion and tribocorrosion behaviour of β-type Ti-Nb and Ti-Mo surfaces designed by diffusion treatments for biomedical applications. *Corros. Sci.* **2018**, *140*, 51−60.

(10) Li, J.; Lin, X.; Guo, P.; Song, M.; Huang, W. Electrochemical behaviour of laser solid formed Ti−6Al−4V alloy in a highly concentrated NaCl solution. *Corros. Sci.* **2018**, *142*, 161−174.

(11) Liu, Y.; Chen, L. F.; Tang, H. P.; Liu, C. T.; Liu, B.; Huang, B. Y. Design of powder metallurgy titanium alloys and composites. *Mater. Sci. Eng., A* **2006**, *418*, 25−35.

(12) Zhang, L. C.; Klemm, D.; Eckert, J.; Hao, Y. L.; Sercombe, T. B. Manufacture by selective laser melting and mechanical behavior of a biomedical Ti−24Nb−4Zr−8Sn alloy. *Scr. Mater.* **2011**, *65*, 21−24.

(13) Guo, Y.; Jia, L.; Kong, B.; Zhang, F.; Liu, J.; Zhang, H. Improvement in the oxidation resistance of Nb-Si based alloy by selective laser melting. *Corros. Sci.* **2017**, *127*, 260−269.

(14) Sanviemvongsak, T.; Monceau, D.; Macquaire, B. High temperature oxidation of IN 718 manufactured by laser beam melting and electron beam melting: Effect of surface topography. *Corros. Sci.* **2018**, *141*, 127−145.

(15) Gong, X.; Li, Y.; Nie, Y.; Huang, Z.; Liu, F.; Huang, L.; Jiang, L.; Mei, H. Corrosion behaviour of CoCrMo alloy fabricated by electron beam melting. *Corros. Sci.* **2018**, *139*, 68−75.

(16) Zhang, L. C.; Sercombe, T. B. Selective laser melting of low-modulus biomedical Ti-24Nb-4Zr-8Sn alloy: effect of laser point distance. *Key Eng. Mater.* **2012**, *520*, 226−233.

(17) Zhang, L. C.; Liu, Y. J.; Li, S. J.; Hao, Y. L. Additive manufacturing of titanium alloys by electron beam melting: A review. *Adv. Eng. Mater.* **2018**, *20*, 1700842.

(18) Liu, Y. J.; Li, S. J.; Hou, W. T.; Wang, S. G.; Hao, Y. L.; Yang, R.; Sercombe, T. B.; Zhang, L. C. Electron beam melted beta-type Ti−24Nb−4Zr−8Sn porous structures with high strength-to-modulus ratio. *J. Mater. Sci. Technol.* **2016**, *32*, 505−508.

(19) Liu, Y. J.; Li, S. J.; Wang, H. L.; Hou, W. T.; Hao, Y. L.; Yang, R.; Sercombe, T. B.; Zhang, L. C. Microstructure, defects and mechanical behavior of beta-type titanium porous structures manufactured by electron beam melting and selective laser melting. *Acta Mater.* **2016**, *113*, 56−67.

(20) Liu, Y. J.; Li, S. J.; Zhang, L. C.; Hao, Y. L.; Sercombe, T. B. Early plastic deformation behaviour and energy absorption in porous β-type biomedical titanium produced by selective laser melting. *Scr. Mater.* **2018**, *153*, 99−103.

(21) Liu, Y. J.; Liu, Z.; Jiang, Y.; Wang, G. W.; Yang, Y.; Zhang, L. C. Gradient in microstructure and mechanical property of selective laser melted AlSi10Mg. *J. Alloys Compd.* **2018**, *735*, 1414−1421.

(22) Zhang, L. C.; Attar, H. Selective laser melting of titanium alloys and titanium matrix composites for biomedical applications: a review. *Adv. Eng. Mater.* **2016**, *18*, 463−475.

(23) Liu, Y. J.; Li, X. P.; Zhang, L. C.; Sercombe, T. B. Processing and properties of topologically optimized biomedical Ti−24Nb−4Zr−8Sn scaffolds manufactured by selective laser melting. *Mater. Sci. Eng., A* **2015**, *642*, 268−278.

(24) Liu, Y. J.; Wang, H. L.; Li, S. J.; Wang, S. G.; Wang, W. J.; Hou, W. T.; Hao, Y. L.; Yang, R.; Zhang, L. C. Compressive and fatigue behavior of beta-type titanium porous structures fabricated by electron beam melting. *Acta Mater.* **2017**, *126*, 58−66.

(25) Martín-Cameán, A.; Jos, Á.; Mellado-García, P.; Iglesias-Linares, A.; Solano, E.; Cameán, A. M. In vitro and in vivo evidence of the cytotoxic and genotoxic effects of metal ions released by orthodontic appliances: A review. *Environ. Toxicol. Pharmacol.* **2015**, *40*, 86−113.

(26) Lu, Y.; Wu, S.; Gan, Y.; Li, J.; Zhao, C.; Zhuo, D.; Lin, J. Investigation on the microstructure, mechanical property and corrosion behavior of the selective laser melted CoCrW alloy for dental application. *Mater. Sci. Eng., C* **2015**, *49*, 517−525.

(27) Choubey, A.; Balasubramaniam, R.; Basu, B. Effect of replacement of V by Nb and Fe on the electrochemical and corrosion behavior of Ti−6Al−4V in simulated physiological environment. *J. Alloys Compd.* **2004**, *381*, 288−294.

(28) Dai, N. W.; Zhang, L. C.; Zhang, J. X.; Chen, Q. M.; Wu, M. L. Corrosion behavior of selective laser melted Ti-6Al-4V alloy in NaCl solution. *Corros. Sci.* **2016**, *102*, 484−489.

(29) Dai, N. W.; Zhang, L. C.; Zhang, J. X.; Zhang, X.; Ni, Q. Z.; Chen, Y.; Wu, M. L.; Yang, C. Distinction in corrosion resistance of selective laser melted Ti-6Al-4V alloy on different planes. *Corros. Sci.* **2016**, *111*, 703−710.

(30) Bai, Y.; Gai, X.; Li, S. J.; Zhang, L. C.; Liu, Y. J.; Hao, Y. L.; Zhang, X.; Yang, R.; Gao, Y. B. Improved corrosion behaviour of electron beam melted Ti-6Al-4V alloy in phosphate buffered saline. *Corros. Sci.* **2017**, *123*, 289−296.

(31) Gong, X.; Cui, Y.; Wei, D.; Liu, B.; Liu, R.; Nie, Y.; Li, Y. Building direction dependence of corrosion resistance property of Ti−6Al−4V alloy fabricated by electron beam melting. *Corros. Sci.* **2017**, *127*, 101−109.

(32) Li, J.; Lin, X.; Zheng, M.; Wang, J.; Guo, P.; Qin, T.; Zhu, M.; Huang, W.; Yang, H. Distinction in anodic dissolution behavior on different planes of laser solid formed Ti-6Al-4V alloy. *Electrochim. Acta* **2018**, *283*, 1482−1489.

(33) Chiu, T. M.; Mahmoudi, M.; Dai, W.; Elwany, A.; Liang, H.; Castaneda, H. Corrosion assessment of Ti-6Al-4V fabricated using laser powder-bed fusion additive manufacturing. *Electrochim. Acta* **2018**, *279*, 143−151.

(34) Dai, N. W.; Zhang, J. X.; Chen, Y.; Zhang, L. C. Heat treatment degrading the corrosion resistance of selective laser melted Ti-6Al-4V alloy. *J. Electrochem. Soc.* **2017**, *164*, C428−C434.

(35) Chen, Y.; Zhang, J. X.; Gu, X. H.; Dai, N. W.; Qin, P.; Zhang, L. C. Distinction of corrosion resistance of selective laser melted Al-12Si alloy on different planes. *J. Alloys Compd.* **2018**, *747*, 648−658.

(36) Yang, Y.; Chen, Y.; Zhang, J. X.; Gu, X. H.; Qin, P.; Dai, N. W.; Li, X. P.; Kruth, J. P.; Zhang, L. C. Improved corrosion behavior of

DOI: 10.1021/acsbiomaterials.8b01341
ACS Biomater. Sci. Eng. 2019, 5, 1141−1149

ultrafine-grained eutectic Al-12Si alloy produced by selective laser melting. *Mater. Des.* **2018**, *146*, 239−248.
(37) Korb, L. J.; Olson, D. L.; Davis, J. R.; Destefani, J. D.; Frissell, H. J.; Crankovic, G. M.; Jenkins, D. M. *ASM Handbook*, 9th ed.; ASM: 1987; Vol. *13*, p 3455.
(38) Chen, Y.; Zhang, J. X.; Dai, N. W.; Qin, P.; Attar, H.; Zhang, L. C. Corrosion behaviour of selective laser melted Ti-TiB biocomposite in simulated body fluid. *Electrochim. Acta* **2017**, *232*, 89−97.
(39) Wan, Q.; Ding, H.; Yousaf, M. I.; Chen, Y. M.; Liu, H. D.; Hu, L.; Yang, B. Corrosion behaviors of tin and Ti-Si-N (with 2.9 atom % and 5.0 atom % Si) coatings by electrochemical impedance spectroscopy. *Thin Solid Films* **2016**, *616*, 601−607.
(40) Galván, J. C.; Larrea, M. T.; Braceras, I.; Multigner, M.; González-Carrasco, J. L. In vitro corrosion behaviour of surgical 316lvm stainless steel modified by Si+ ion implantation − An electrochemical impedance spectroscopy study. *J. Alloys Compd.* **2016**, *676*, 414−427.
(41) Jia, Z.; Duan, X. G.; Qin, P.; Zhang, W. C.; Wang, W. M.; Yang, C.; Sun, H. Q.; Wang, S. B.; Zhang, L. C. Disordered atomic packing structure of metallic glass: Toward ultrafast hydroxyl radicals production rate and strong electron transfer ability in catalytic performance. *Adv. Funct. Mater.* **2017**, *27*, 1702258.
(42) Liang, S. X.; Jia, Z.; Liu, Y. J.; Zhang, W.; Wang, W.; Lu, J.; Zhang, L. C. Compelling Rejuvenated Catalytic Performance in Metallic Glasses. *Adv. Mater.* **2018**, *30*, 1802764.
(43) Alves, A. C.; Wenger, F.; Ponthiaux, P.; Celis, J. P.; Pinto, A. M.; Rocha, L. A.; Fernandes, J. C. S. Corrosion mechanisms in titanium oxide-based films produced by anodic treatment. *Electrochim. Acta* **2017**, *234*, 16−27.
(44) Alves, V. A.; Reis, R. Q.; Santos, I. C. B.; Souza, D. G.; de F. Gonçalves, T.; Pereira-da-Silva, M. A.; Rossi, A.; da Silva, L. A. In situ impedance spectroscopy study of the electrochemical corrosion of Ti and Ti−6Al−4V in simulated body fluid at 25°C and 37°C. *Corros. Sci.* **2009**, *51*, 2473−2482.
(45) Tamilselvi, S.; Raman, V.; Rajendran, N. Corrosion behaviour of Ti−6Al−7Nb and Ti−6Al−4V eli alloys in the simulated body fluid solution by electrochemical impedance spectroscopy. *Electrochim. Acta* **2006**, *52*, 839−846.
(46) Qin, P.; Liu, Y. J.; Sercombe, T. B.; Li, Y. H.; Zhang, C. W.; Cao, C. D.; Sun, H. Q.; Zhang, L. C. Improved corrosion resistance on selective laser melting produced Ti-5Cu alloy after heat treatment. *ACS Biomater. Sci. Eng.* **2018**, *4*, 2633−2642.
(47) Guan, L.; Li, Y.; Wang, G.; Zhang, Y.; Zhang, L. C. pH dependent passivation behavior of niobium in acid fluoride-containing solutions. *Electrochim. Acta* **2018**, *285*, 172−184.
(48) Coelho, L. B.; Cossement, D.; Olivier, M. G. Benzotriazole and cerium chloride as corrosion inhibitors for AA2024-T3: An EIS investigation supported by SVET and ToF-SIMS analysis. *Corros. Sci.* **2018**, *130*, 177−189.
(49) Huttunen-Saarivirta, E.; Rajala, P.; Bomberg, M.; Carpén, L. EIS study on aerobic corrosion of copper in ground water: influence of micro-organisms. *Electrochim. Acta* **2017**, *240*, 163−174.
(50) Bandeira, R. M.; van Drunen, J.; Garcia, A. C.; Tremiliosi-Filho, G. Influence of the thickness and roughness of polyaniline coatings on corrosion protection of AA7075 aluminum alloy. *Electrochim. Acta* **2017**, *240*, 215−224.
(51) N, P. *Electrochemistry and Corrosion Science*; Kluwer Academic Publishers: New York, 2004; p 362.
(52) Li, J.; Bai, Y.; Fan, Z.; Li, S.; Hao, Y.; Yang, R.; Gao, Y. Effect of fluoride on the corrosion behavior of nanostructured Ti-24Nb-4Zr-8Sn alloy in acidulated artificial saliva. *J. Mater. Sci. Technol.* **2018**, *34*, 1660−1670.
(53) Zhang, Y.; Davenport, A. J.; Burke, B.; Vyas, N.; Addison, O. Effect of Zr addition on the corrosion of Ti in acidic and reactive oxygen species (ROS)-containing environments. *ACS Biomater. Sci. Eng.* **2018**, *4*, 1103.
(54) Navarro Laboulais, J.; Amigó Mata, A.; Amigó Borrás, V.; Igual Muñoz, A. Electrochemical characterization and passivation behaviour of new beta-titanium alloys (Ti35Nb10Ta-xFe). *Electrochim. Acta* **2017**, *227*, 410−418.
(55) Bai, Y.; Deng, Y.; Zheng, Y.; Li, Y.; Zhang, R.; Lv, Y.; Zhao, Q.; Wei, S. Characterization, corrosion behavior, cellular response and in vivo bone tissue compatibility of titanium−niobium alloy with low Young's modulus. *Mater. Sci. Eng., C* **2016**, *59*, 565−576.

DOI: 10.1021/acsbiomaterials.8b01341
ACS Biomater. Sci. Eng. 2019, 5, 1141−1149